Journal of Non-Newtonian Fluid Mechanics 319 (2023) 105072

Contents lists available at ScienceDirect

Journal of Non-Newtonian Fluid Mechanics

journal homepage: www.elsevier.com/locate/jnnfm

Spatio-temporal instabilities in viscoelastic channel flows: The centre mode

Dongdong Wan [a], Guangrui Sun [a], Duo Xu [b,c], Mengqi Zhang [a,*], Chang Shu [a]

[a] Department of Mechanical Engineering, National University of Singapore, 9 Engineering Drive 1, Singapore, 117575, Singapore
[b] The State Key Laboratory of Nonlinear Mechanics, Institute of Mechanics, Chinese Academy of Sciences, Beijing, 100190, PR China
[c] School of Engineering Science, University of Chinese Academy of Sciences, Beijing, 100049, PR China

ARTICLE INFO

Keywords:
Viscoelastic fluids
Channel flows
Spatio-temporal instability
Ginzburg–Landau equation

ABSTRACT

We study in this work the spatio-temporal characteristics of the centre-mode linear instability in viscoelastic channel flows of Oldroyd-B and FENE-P fluids. The linear complex Ginzburg–Landau equation derived using an amplitude expansion method is adopted to determine whether the flow is convectively unstable or absolutely unstable. Comparison of the obtained results with those from the conventional saddle-point searching method shows a favourable agreement. This demonstrates the good predictability of the linear complex Ginzburg–Landau equation which is more suitable for a parametric study in a large space than the conventional method. We found that the centre-mode instability in the viscoelastic channel flow is of a convective nature, i.e., the trailing edge of the wavepacket travels downstream. This could be attributed to the relatively high phase speed, low spreading rate and low growth rate of the instability, collectively preventing a disturbance from travelling upstream. Our results show that stronger polymer elasticity (a greater elasticity number or larger polymer concentration) marginally affects the trailing-edge velocity of the centre mode. Decreasing the maximum polymer extensibility in the FENE-P model reduces the spreading rate of the wavepacket and makes the centre-mode disturbance more convective. Theoretical derivations at asymptotically high Reynolds numbers confirm the convective nature of the instabilities from numerical observations. Our results may be conducive to a better understanding of the spatio-temporal instability in viscoelastic experiments.

1. Introduction

As a typical type of viscoelastic fluids, polymeric solutions can be obtained via an addition of a small amount of long-chain flexible polymers into a Newtonian solvent. A well-known phenomenon of the polymeric flow is the significant turbulent drag reduction up to 80% [1,2]. Drag reducing techniques using polymers have since been extensively tested and developed, including applications in crude-oil pipelines [3], sewerages [4], on the marine vehicle hull [5], etc. Meanwhile, the mechanisms underlying the turbulent drag reduction by polymers have also been intriguing researchers for a long time [6,7]. In recent times the onset of the viscoelastic turbulence, particularly the flow instability, has received increasing attention [8,9].

In the last few years, because of its relevance to the maximal drag reduction asymptote, the discovery and characterisation of the elasto-inertial turbulence (EIT) has significantly boosted the community's interest in studying the flow transition to EIT [10–13]. The transition mechanism in the EIT is currently under active investigations. Graham and coworkers proposed a wall-mode transition route based on the viscoelastically-modified Tollmien–Schlichting wave [14–16]. Meanwhile, a novel centre-mode linear instability has been found in a series of works (see the next section for a detailed summary). However, this newly-found linear instability has so far solely been studied in a *temporal* framework, i.e., only the ultimate fate of the *global* disturbance is concerned at an asymptotically long time. In realistic flow systems, the disturbances in the environment as well as imperfections of the geometries are, however, *local* in nature. These noise signals can be spatially amplified as they are convected downstream and the resultant spatial pattern can play a role in the flow dynamics [17,18]. Imposition of a local disturbance on viscoelastic flows has also been considered recently by Hariharan et al. [19] and Shnapp & Steinberg [20] with new discoveries of the elastic effect on the spatio-temporal development of the disturbance. Characterisation of the linear instability in a *spatio-temporal* framework is thus important and needed to be performed to further our understanding of the transition process in the EIT flow. In this work, we will examine the spatio-temporal instabilities of the centre mode in viscoelastic plane Poiseuille flows. Below, we will first present a literature survey on the centre-mode instability in viscoelastic flows, and then review studies on the spatio-temporal instabilities in various viscoelastic flows.

* Corresponding author.
E-mail address: mpezmq@nus.edu.sg (M. Zhang).

https://doi.org/10.1016/j.jnnfm.2023.105072
Received 2 March 2023; Accepted 24 May 2023
Available online 1 June 2023

1.1. Centre-mode instability in viscoelastic flows

The centre mode in the transition of viscoelastic Poiseuille flows has been studied from various perspectives, including modal and non-modal stability analyses, primary bifurcation analysis in a weakly nonlinear framework, finite-amplitude exact coherent structures (ECSs), etc.

The centre-mode linear instability was first revealed numerically by Garg et al. [21] in viscoelastic pipe flows of Oldroyd-B fluids. They attributed this instability to a subtle balance of the effects of fluid inertia, viscosity and polymer elasticity. Later, Khalid et al. [22] showed more systematically the sole existence of the centre-mode instability only at $\beta \gtrsim 0.5$ in the viscoelastic channel flow (where β is the viscosity ratio related to the polymer concentration). On the other hand, Chaudary et al. [23] found that the instability persists down to very small values of $\beta = O(0.001)$ in the pipe counterpart. Subsequently, Wan et al. [24] discovered centre-mode instability in the UCM limit for the pipe flow (i.e., $\beta = 0$; see their Appendix E), helping to complete the instability picture in the parameter space. Zhang [25]'s calculation showed that the modal linear instability of the centre mode is also accompanied by a strong non-modal energy growth in the viscoelastic pipe flows. Scaling laws for the linear critical conditions have also been reported in the linear stability analysis of Garg et al. [21] for the viscoelastic pipe flows. These scaling laws were later revisited by Dong & Zhang [26] using an asymptotic analysis and extended to the weakly nonlinear regime in Wan et al. [27].

Experimental evidence for the centre-mode instability has been given by Choueiri et al. [13] in a controlled environment. However, a clean background with a low noise level is often not the case in real-world situations, rendering the supercritical excitation of this instability mode rare. The first nonlinear study of the centre mode by Page et al. [28] addressed exactly this problem by showcasing the existence of ECSs born from the centre mode in strongly subcritical parameter regime of viscoelastic channel flows of FENE-P fluids (i.e., the flow is linearly stable but nonlinearly unstable), in addition to the supercritical route [21]. This study was further corroborated by Buza et al. [29] using a branch continuation approach. Such a coexistence of both supercritical and subcritical bifurcations in the fluid system has also been confirmed in a weakly nonlinear framework by Buza et al. [30] (for channel flows using the FENE-P model) and by Wan et al. [24] (for pipe flows based on the Oldroyd-B model). Additionally, finite-amplitude travelling wave solutions (a kind of ECS) were found to persist even down to the inertialess limit [29,31] in viscoelastic channel flows, extending again the linear instability in this limit discussed by Khalid et al. [32]. Nevertheless, the ECSs in viscoelastic pipe flows have yet not been reported in the literature.

As we can see, in the current research on the centre-mode instability, the linear stability analyses only concern the temporal stability. As discussed earlier, the spatio-temporal characteristics of the instability are also important and should be understood. Next, we will summarise previous works on the spatio-temporal analyses of the viscoelastic flows and then explain our research motivation in this work.

1.2. Absolute/convective instabilities in viscoelastic flows

The spatio-temporal instability in a flow system can be characterised by distinguishing between absolute instability (AI) and convective instability (CI). This distinction was originally made by the plasma physicists [33] and later introduced into the hydrodynamics community by Huerre & Monkewitz among others. The AICI property of a flow can be determined by examining the spatio-temporal evolution of an initially localised infinitesimally small disturbance imposed on the laminar base flow. At an asymptotically long time, if the disturbance grows at any fixed location in the stationary frame, the flow is said to be absolutely unstable; in this case, the initially localised disturbance spreads both upstream and downstream, gradually contaminating the whole geometry. On the contrary, if the disturbance decays at any fixed location in the stationary frame (when the time is large) and its growth can only be observed in some moving frames, the flow is said to be convectively unstable, i.e., the disturbance is swept away from its original location by the laminar base flow. The disturbance does not propagate upstream in this case.

The AICI of viscoelastic flows have been investigated in a variety of flow configurations in the past decades, including jets, mixing layers, wake flows, mixed convection flows and so on. Concerning planar viscoelastic jets, Ray & Zaki [34] demonstrated in an AICI analysis that the single-stream jet of FENE-P fluids is absolutely unstable when the elastic effect is sufficiently strong and the shear layer is thin enough. For viscoelastic mixing layers (also known as free shear layers), using the Oldroyd-B model, Sircar & Bansal [35] reported that the flow instability is purely absolute at a viscosity ratio of $\beta = 0.35$, while AI and CI coexist at $\beta = 0.20$. Later, the authors extended their analysis to the linear PTT model [36] to account for the shear-thinning effect. Their instability diagram showed that for sufficiently strong elasticity (characterised by the elasticity number E) the flow is always absolutely unstable and that the flow can only be convectively unstable in a narrow region of small E [37].

The AICI analysis has also been applied to wall-bounded viscoelastic flows. In the Rayleigh–Bénard–Poiseuille mixed convection with polymers, the analyses by Hirata et al. [38] demonstrated a coexistence of AI and CI in the parameter space. Recently, Qin et al. [39] conducted experiments on the viscoelastic flow around a confined cylinder. The elastic wave in the flow was found to travel upstream and its speed increases with the Weissenberg number Wi, suggestive of an absolute instability in the flow. Returning to the rectilinear flow configuration, the latest work by Shnapp & Steinberg [20] studies the spatio-temporal development of the disturbance in a canonical viscoelastic shear flow. They observed that a single initial impulse can excite multiple pulses downstream at high Wi, signifying a novel pulse-splitting transition route to elastic turbulence. It should be noted that their experiments were conducted in the strongly-elastic inertialess regime ($Re \approx 0$, which is not the case considered in the current work), and their focus is also not on the determination of AICI in a large parameter space.

1.3. The position and structure of the current work

The literature review detailed above has pointed to a research gap due to a missing study on the absolute/convective instabilities in viscoelastic channel flows. Such a work is properly needed as it can supplement the ongoing temporal analyses of the viscoelastic flows and help us to understand more completely the linear dynamics of these flows. Knowledge of the spatio-temporal characteristics of the unstable flow system is also helpful for experimental diagnostics and flow control as well as for understanding the associated pattern and the chaotic behaviours in the flow [18]. Besides, experimental work on the AICI in viscoelastic channel flow has started to be reported [20]; our work may provide a timely analysis tool to understand future experimental observations.

The rest of the paper is organised as follows. In Section 2 we introduce the governing equations and the important parameters in the viscoelastic channel flow. We will describe in detail two methods for the spatio-temporal analysis, i.e., the method of locating saddle points in a complex wavenumber plane and that using the linear complex Ginzburg–Landau equation. Implementation of the numerical methods is briefly explained in Section 3. We present the results in Section 4, including the validation of the numerical methods and the AICI of the centre-mode instabilities. Section 5 concludes the paper with a summary of the main findings and some discussions on the flow physics.

2. Problem formulation

2.1. Governing equations and parameters

The hydrodynamic stability analysis is applied to a pressure-driven viscoelastic flow of FENE-P (finitely extensible nonlinear elastic model with Peterlin closure) fluids in a rigid stationary channel (plane Poiseuille flow). The channel has a half height of H in the vertical direction and is infinite in the other two directions in a Cartesian coordinate system (with x, y and z denoting the streamwise, wall-normal and spanwise directions, respectively). The fluid is characterised by a density of ρ and a dynamic viscosity of $\mu = \mu_s + \mu_p$ with μ_s and μ_p being the viscosities due to the solvent and polymers respectively. At the centreline of the channel, the Newtonian Poiseuille flow has the velocity U_c and its viscoelastic counterpart will have a slightly larger value due to the nonlinear model of FENE-P, to be discussed shortly. Quantities used to nondimensionalise the governing equations of the flow include the length scale H, velocity scale U_c, reference pressure ρU_c^2 and reference polymeric stress $\mu_p U_c/H$.

The nondimensional nonlinear governing equations are given as

$$\boldsymbol{\nabla}\cdot\hat{\boldsymbol{u}} = 0, \quad \frac{\partial\hat{\boldsymbol{u}}}{\partial t} + \hat{\boldsymbol{u}}\cdot\boldsymbol{\nabla}\hat{\boldsymbol{u}} = -\boldsymbol{\nabla}\hat{p} + \frac{\beta}{Re}\nabla^2\hat{\boldsymbol{u}} + \frac{1-\beta}{Re}\boldsymbol{\nabla}\cdot\hat{\boldsymbol{\tau}}_p, \tag{1a,b}$$

$$\frac{\partial\hat{\boldsymbol{c}}}{\partial t} + \hat{\boldsymbol{u}}\cdot\boldsymbol{\nabla}\hat{\boldsymbol{c}} - \hat{\boldsymbol{c}}\cdot\boldsymbol{\nabla}\hat{\boldsymbol{u}} - (\boldsymbol{\nabla}\hat{\boldsymbol{u}})^T\cdot\hat{\boldsymbol{c}} = -\hat{\boldsymbol{\tau}}_p, \tag{1c}$$

where the velocity vector $\hat{\boldsymbol{u}} = (\hat{u}_x, \hat{u}_y, \hat{u}_z)$, $\hat{p}$ is the pressure, $\hat{\boldsymbol{\tau}}_p$ is the polymeric stress tensor and the conformation tensor $\hat{\boldsymbol{c}} = (\hat{c}_{xx}, \hat{c}_{xy}, \hat{c}_{xz}, \hat{c}_{yy}, \hat{c}_{yz}, \hat{c}_{zz})$. The FENE-P model reads [40]

$$\hat{\boldsymbol{\tau}}_p = \frac{f(\hat{\boldsymbol{c}})\hat{\boldsymbol{c}} - \boldsymbol{I}}{Wi} \quad \text{with} \quad f(\hat{\boldsymbol{c}}) = \frac{1}{1 - \mathrm{tr}(\hat{\boldsymbol{c}})/L^2} \tag{2}$$

being the Peterlin function, where L is the maximally allowed extension of polymers in a statistical sense and $\boldsymbol{I}$ is the identity tensor. This model is adopted for its ability to capture some of the most important flow behaviours like the shear thinning [41] and drag reduction [42]. It has been widely used in the stability analyses and numerical simulations of viscoelastic flows ([10,14,28,43,44] among others). The FENE-P model reduces to the Oldroyd-B fluid model when $L \to \infty$. In addition to L, the control parameters also include the Reynolds number $Re = \rho U_c H/\mu$, the Weissenberg number $Wi = \lambda U_c/H$ (where λ is the longest polymer relaxation time) and the viscosity ratio $\beta = \mu_s/\mu$. The case $\beta = 1$ corresponds to the Newtonian fluid and $\beta = 0$ the UCM fluid. We also use the elasticity number in the following, defined as $E \equiv Wi/Re = \lambda\mu/(\rho H^2)$, which only depends on the fluid properties and flow geometry.

The governing Eqs. (1) with no-slip boundary conditions $\hat{\boldsymbol{u}}(y = \pm 1) = \boldsymbol{0}$ admit an analytical steady solution $\boldsymbol{U} = (U, 0, 0)$, $P = P(x)$ and $\boldsymbol{C} = (C_{xx}, C_{xy}, 0, C_{yy}, 0, C_{zz})$ with the components being [45]

$$U(y) = -\frac{Re}{2\beta}\frac{\mathrm{d}P}{\mathrm{d}x}\left(1 - y^2\right) - \frac{3(1-\beta)}{8K_0\beta}[G(y) - G(-1)], \tag{3a}$$

$$C_{xx}(y) = \frac{1 + 2Wi^2T_{xy}^2(y)}{F(y)}, \; C_{xy}(y) = \frac{WiT_{xy}(y)}{F(y)}, \; C_{yy}(y) = \frac{1}{F(y)}, \; C_{zz}(y) = \frac{1}{F(y)}, \tag{3b}$$

where

$$G(y) = [K_0 y + J(y)]^{\frac{1}{3}}[3K_0 y - J(y)] + [K_0 y - J(y)]^{\frac{1}{3}}[3K_0 y + J(y)],$$
$$F(y) = 1 + \frac{2Wi^2T_{xy}^2(y)}{L^2} + \frac{3}{L^2}, \quad T_{xy}(y) = [K_0 y + J(y)]^{\frac{1}{3}} + [K_0 y - J(y)]^{\frac{1}{3}},$$
$$J(y) = \sqrt{K_0^2 y^2 + K_1^3}, \quad K_0 = \frac{ReL^2}{4\beta Wi^2}\frac{\mathrm{d}P}{\mathrm{d}x}, \quad K_1 = \frac{L^2}{6Wi^2}\left(\frac{3}{L^2} + \frac{1}{\beta}\right). \tag{4}$$

The solution (3) constitutes the laminar base flow in our stability analysis. One can set the pressure gradient to be $\frac{\mathrm{d}P}{\mathrm{d}x} = -\frac{2}{Re}$ so as to recover the parabolic velocity profile $U_c = 1 - y^2$ when $\beta = 1$.

To perform the linear spatio-temporal analysis of the flow, we decompose the dependent variables in (1) into their laminar base flow states and infinitesimal perturbations as $\hat{\boldsymbol{u}} = \boldsymbol{U} + \boldsymbol{u}$, $\hat{p} = P + p$, $\hat{\boldsymbol{\tau}}_p = \boldsymbol{T} + \boldsymbol{\tau}$ and $\hat{\boldsymbol{c}} = \boldsymbol{C} + \boldsymbol{c}$. Inserting these decompositions into (1) and linearising the equations about the laminar base flow solution lead to the perturbation equations

$$\boldsymbol{\nabla}\cdot\boldsymbol{u} = 0, \; \frac{\partial\boldsymbol{u}}{\partial t} + \boldsymbol{u}\cdot\boldsymbol{\nabla}\boldsymbol{U} + \boldsymbol{U}\cdot\boldsymbol{\nabla}\boldsymbol{u} = -\boldsymbol{\nabla}p + \frac{\beta}{Re}\nabla^2\boldsymbol{u} + \frac{1-\beta}{ReWi}\boldsymbol{\nabla}\cdot(f_0\boldsymbol{c} + f_1\boldsymbol{C}), \tag{5a,b}$$

$$\frac{\partial\boldsymbol{c}}{\partial t} + \boldsymbol{u}\cdot\boldsymbol{\nabla}\boldsymbol{C} - \boldsymbol{c}\cdot\boldsymbol{\nabla}\boldsymbol{U} - (\boldsymbol{\nabla}\boldsymbol{u})^T\cdot\boldsymbol{C} + \boldsymbol{U}\cdot\boldsymbol{\nabla}\boldsymbol{c} - \boldsymbol{C}\cdot\boldsymbol{\nabla}\boldsymbol{u} - (\boldsymbol{\nabla}\boldsymbol{U})^T\cdot\boldsymbol{c} = -\frac{f_0\boldsymbol{c} + f_1\boldsymbol{C}}{Wi}, \tag{5c}$$

along with no-slip boundary conditions $\boldsymbol{u}(y = \pm 1) = \boldsymbol{0}$ at the channel wall (it should be noted that there is no need to specify any boundary condition for $\boldsymbol{c}$ because no $\partial\boldsymbol{c}/\partial y$ terms exist in (5c). Here for the nonlinear Peterlin closure, the linearisation based on the first-order Taylor expansion at $f(\boldsymbol{C})$ gives

$$f(\hat{\boldsymbol{c}}) = f(\boldsymbol{C} + \boldsymbol{c}) \approx f(\boldsymbol{C}) + \frac{\partial f(\boldsymbol{C})}{\partial C_{xx}}c_{xx} + \frac{\partial f(\boldsymbol{C})}{\partial C_{yy}}c_{yy} + \frac{\partial f(\boldsymbol{C})}{\partial C_{zz}}c_{zz} = f_0 + f_1, \tag{6}$$

with $f_0 = f(\boldsymbol{C})$ and $f_1 = f_0^2\mathrm{tr}(\boldsymbol{c})/L^2$.

A numerical observation by Zhang et al. [43] on the FENE-P Poiseuille flow indicated that compared to 3-D disturbance, the 2-D disturbance first becomes unstable (whereas for the Oldroyd-B fluids, an analytical derivation for Squire's theorem can be found in Ref. [46]). This validates a 2-D analysis in the present study. By writing the state vector $\boldsymbol{\gamma} = (u_x, u_y, p, c_{xx}, c_{xy}, c_{yy}, c_{zz})^{\mathrm{T}}$ for the 2-D disturbance, the linear equation system in (5) can be recast into a compact form of

$$\boldsymbol{M}\frac{\partial\boldsymbol{\gamma}}{\partial t} = \boldsymbol{L}\boldsymbol{\gamma}, \tag{7}$$

where $\boldsymbol{M}$ and $\boldsymbol{L}$ can be readily derived by matching (7) and (5).

2.2. Spatio-temporal analysis of the viscoelastic channel flow

In this section, we introduce two techniques (i.e., the saddle-point searching method and the method based on the linear complex Ginzburg–Landau equation) to characterise the spatio-temporal instability of a flow. Our focus is on the determination of the absolute or convective nature of the instability. We set out the presentation by stating that the two methods well provide consistent predictions of the AICI property of the centre mode in the viscoelastic rectilinear flow; the method based on the linear complex Ginzburg–Landau equation is more suitable for an exploration in a larger parameter space. One of the contributions of this work is to apply the linear complex Ginzburg–Landau equation to probe the spatio-temporal characteristics in this flow.

2.2.1. Locating the saddle point in the eigenvalue problem

In determining the AICI of a disturbed flow system, one conventionally follows the method introduced by Huerre & Monkewitz [47] to identify saddle points in a complex wavenumber plane (see their comprehensive review [18]). In this method, the linear impulse response of a laminar flow can be described by Green's function $G(x, t)$ in the form of a wavepacket. By applying the steepest descent method to $G(x, t)$, one can obtain its long-time behaviour dominated by the characteristics of the saddle points along various rays like $(x - x_0)/t = \text{Const.}$ (x_0: the initial location of the impulse). The growth rate at the saddle point along the ray $(x - x_0)/t = 0$ (i.e., at any fixed location x when $t \to \infty$) corresponds to the (maximal) absolute growth rate. If this absolute growth rate is negative (positive), the flow instability is said to be CI (AI). This method only requires solving the linear eigenvalue problem in the complex frequency and complex wavenumber space. The mathematical procedure in determining the AICI of a flow using this method is described as follows.

Assuming for Eq. (7) a wave-like solution

$$\boldsymbol{\gamma} = \tilde{\boldsymbol{\gamma}}e^{i\alpha x + \mu t} + \text{c.c.}, \tag{8}$$

where $\tilde{\boldsymbol{\gamma}}$ is the shape function, $\alpha = \alpha_r + i\alpha_i$ is the complex-valued wavenumber, $\mu = \mu(\alpha) = \mu_r + i\mu_i$ is the eigenvalue with μ_r being the linear growth rate and μ_i the frequency, and c.c. stands for the complex conjugate of its preceding term. The complex phase speed c is related to μ as $\mu = -i\alpha c$. Inserting (8) into (7) leads to the linear eigenvalue problem

$$\mu\widetilde{\boldsymbol{M}}\tilde{\boldsymbol{\gamma}} = \widetilde{\boldsymbol{L}}\tilde{\boldsymbol{\gamma}}, \tag{9}$$

where $\widetilde{\boldsymbol{M}}$ and $\widetilde{\boldsymbol{L}}$ are corresponding operators of $\boldsymbol{M}$ and $\boldsymbol{L}$ in the spectral space.

The AICI property can be determined by locating the saddle point of μ_r in the complex wavenumber plane in the laboratory frame, satisfying the pinching condition [18,47]. We however found that the saddle point in the viscoelastic flows is located far away from the real axis in the complex wavenumber plane, making it difficult to find the saddle point. Suslov [48] also noted that for strong through flows the saddle point may be difficult to identify in the complex wavenumber plane in a laboratory frame. In our work, we follow the method of Ref. [49] to examine the wave growth in a moving frame with axial coordinate x_{m} and velocity v by setting $x - vt = x_{\mathrm{m}}$ in (8). Then the complex growth rate λ observed in the moving frame at asymptotically long time and the corresponding saddle point α_s can be obtained as

$$\lambda(\alpha, v) = \mu(\alpha) + i\alpha v, \quad \left.\frac{\partial\lambda}{\partial\alpha}\right|_{\alpha_s} = 0. \tag{10}$$

The AICI property can now be determined as follows. The complex growth rate at the saddle point is denoted as $\lambda_s(\alpha_s, v)$. If its real part $\lambda_{s,r} > 0$, the wave growth can be observed in the moving frame of velocity v. Otherwise, the wave decays in the moving frame. For linearly unstable flows, we can always find two roots of the equation $\lambda_{s,r}(\alpha_s(v), v) = 0$. One root corresponds to the velocity of the trailing edge v_- of the wavepacket and the other the leading edge v_+. Here v_+ is always positive, i.e., the wave front propagates in the same direction as the laminar base flow. If $v_- > 0$, the whole wavepacket moves downstream, indicating a convective instability; on the contrary, $v_- < 0$ means that the wave trailing edge travels upstream and can spread across the whole channel, corresponding to an absolute instability.

However, some additional difficulties prevented us to use this method extensively in our work (especially when we do the parametric study of the centre mode). One of the difficulties is that the centre-mode instability in viscoelastic flows is characterised by strong elasticity. Numerically resolving a strongly-elastic centre mode is time-consuming, requiring a high resolution even in the spectral method. In addition to this, in the saddle-point searching method, a sufficiently large area in the complex wavenumber plane should be resolved, i.e., one needs to calculate many data points (each being costly), in order to find one genuine saddle point. These factors give rise to a low efficiency of using this method to determine the AICI of the centre mode.

2.2.2. Amplitude expansion: linear complex Ginzburg–Landau equation

To overcome the above-discussed difficulty of applying the traditional AICI method, we will adopt the linear complex Ginzburg–Landau equation (CGLE) in this work to study the AICI in viscoelastic channel flows. This equation serves as an approximate model describing the spatio-temporal evolution of a small disturbance. This equation can be used to evaluate the absolute growth rate (i.e., in the laboratory frame) to determine the AICI. For example, Gao et al. [50] adopted this method in their study of the natural convection of air between two vertical plates and found that the corresponding absolute growth rate is positive, confirming the absolute instability reported in Ref. [51] where the saddle-point searching method was used. Alternatively, the AICI property can also be determined from the linear CGLE by calculating the velocities of the trailing edge and leading edge of the wavepacket [52]. Although this method only gives a second-order approximation of the linear dispersion relation, it proves to be a sufficient analysis tool to reliably determine the AICI properties of the viscoelastic channel flow. This method has been applied successfully to study the AICI in an electrohydrodynamic flow subjected to a Poiseuille flow by Feng et al. [53].

The CGLE can be formally derived in a weakly nonlinear analysis of a flow [54–56] via a multiple-scale expansion of the perturbation equation in the neighbourhood of linear critical conditions. An alternative is the amplitude expansion method which is valid even away from the linear critical conditions as long as the amplitude is not too large to invalidate the expansion. This method was originally proposed by Watson [57] for a weakly nonlinear analysis of Newtonian channel flow, and has been further developed and applied in many other studies [56,58–62]. Conventionally, the amplitude expansion method will give rise to a truncated Stuart–Landau equation (without a spatial derivative term compared to the CGLE). Feng et al. [53] incorporated the spatial-derivative term into their amplitude expansion of electrohydrodynamic flows, enabling a spatio-temporal analysis of the first-order disturbance. Their results demonstrate a favourable agreement between the predictions of AICI from the amplitude expansion method and those from direct numerical simulations (see their Table B.2) even away from the linear critical conditions.

Since the present work is dedicated to the determination of the AICI in the linear regime, we will not follow the conventional procedure to derive the nonlinear CGLE first and then linearise it. We note that many studies have demonstrated that the (relatively weak) nonlinearity will not influence significantly the front propagation speed, but saturate the wave amplitude. This means that the results of linear AICI will likely translate into the nonlinear regime in such flow scenarios, for instance, the wake flow [63], the Blasius boundary layer [64], the mixing layer [65] and the electrohydrodynamic flow [53]. Thus, we can simply only derive the linear terms in the CGLE governing the disturbance amplitude $A = A(x, t)$ as

$$\frac{\partial A}{\partial t} = -c_g\frac{\partial A}{\partial x} + a_1 A + a_2\frac{\partial^2 A}{\partial x^2}. \tag{11}$$

Here c_g is the group velocity, a_1 is the complex growth rate and a_2 is the diffusion coefficient (see Appendix A for the calculation of these three coefficients in the spectral space based on the amplitude expansion method).

The three coefficients in (11) can be approximated based on the linear dispersion relation [55] of the eigenvalue problem (9) using real-valued wavenumber α. The relations are given as

$$c_g \approx i\left.\frac{\partial\mu}{\partial\alpha}\right|_{\alpha_m}, \quad a_1 = \mu|_{\alpha_m}, \quad a_2 \approx -\frac{1}{2}\left.\frac{\partial^2\mu}{\partial\alpha^2}\right|_{\alpha_m}. \tag{12a,b,c}$$

It should be noted that at a given set of control parameters (β, E, Re, L), the coefficients in (11) and (12) should always be evaluated at the wavenumber $\alpha = \alpha_m$ where α_m corresponds to the largest linear growth rate. In this way, the group velocity c_g is real-valued. We will use these relations in Section 4.1 to validate our calculations using the amplitude expansion method.

Following the spatio-temporal analysis in Ref. [52], we can rewrite the linear CGLE (11) in a moving frame with velocity v and the axial coordinate $x_m = x - vt$ as

$$\frac{\partial A}{\partial t} = -(c_g - v)\frac{\partial A}{\partial x_m} + a_1 A + a_2\frac{\partial^2 A}{\partial x_m^2}. \tag{13}$$

By assuming the normal mode form for the solution $A = \tilde{A}e^{i\breve{\alpha}x_m - i\omega t}$, we can obtain the following dispersion relation of the linear CGLE

$$D(\omega, \breve{\alpha}) \equiv -\omega + (c_g - v)\breve{\alpha} + ia_1 - ia_2\breve{\alpha}^2 = 0, \tag{14}$$

where $\breve{\alpha}$ is the modulation wavenumber of the first harmonic with wavenumber α_m, and ω is the complex frequency. There is an equilibrium in $D(\omega, \breve{\alpha})$ given by the condition $(\partial\omega/\partial\breve{\alpha})|_{\breve{\alpha}_e} = 0$, which results in $\breve{\alpha}_e = (c_g - v)/(2ia_2)$. It should be mentioned that $(\breve{\alpha}_e + \alpha_m)$ directly serves as an approximation of the saddle point $\alpha_s(v)$ defined in Section 2.2.1. At this equilibrium, the complex frequency ω_e and its imaginary part

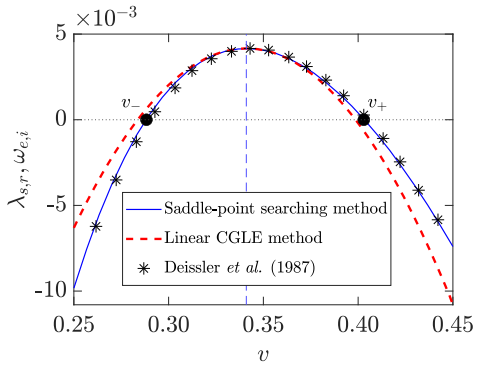

Fig. 1. Validation of the predictions of the spatio-temporal growth rate as a function of the frame moving velocity v in the Newtonian plane Poiseuille flow at $Re = 10000$. The linear instability pertains to a wall mode. The vertical line corresponds to the group velocity $c_g \approx 0.341$. The two black dots mark the trailing-edge velocity v_- and the leading-edge velocity v_+ respectively of the wavepacket.

$\omega_{e,i}$ (i.e., the linear growth rate of the wave observed in the moving frame of velocity v) are

$$\omega_e \equiv \omega(\check{\alpha}_e) = i\left[a_1 - \frac{(c_g - v)^2}{4a_2}\right], \qquad \omega_{e,i} = a_{1r} - \frac{(c_g - v)^2 a_{2r}}{4|a_2|^2}. \tag{15a,b}$$

Here a_{2r} will be positive in the flow system considered here because the linear growth rate μ_r as a function of α can be approximated by a parabola opening downwards, see equation (12c) and Fig. 3(a). From the expression of $\omega_{e,i}$, we know that the maximum linear growth rate $\omega_{e,i} = a_{1r}$ can be observed in the frame moving with velocity $v = c_g$ (note its relevance to the saddle-point searching method). If $a_{1r} > 0$, the flow is linearly unstable; otherwise, it is linearly stable. In the former case, by equating (15b) to zero, the trailing-edge velocity v_- and the leading-edge velocity v_+ of the wavepacket can be obtained as

$$v_- = c_g - \sqrt{\frac{4|a_2|^2 a_{1r}}{a_{2r}}}, \qquad v_+ = c_g + \sqrt{\frac{4|a_2|^2 a_{1r}}{a_{2r}}}. \tag{16a,b}$$

Then the spreading rate of the wavepacket is

$$v_s \equiv v_+ - v_- = 4\sqrt{\frac{|a_2|^2 a_{1r}}{a_{2r}}}. \tag{17}$$

As pointed out in Section 2.2.1, v_+ is always positive, and the flow instability is convective (absolute) when $v_- > 0$ ($v_- < 0$).

3. Numerical methods

A spectral collocation method is adopted and implemented in MATLAB to solve Eq. (9) (for locating the saddle points) and Eqs. (A.3a), (A.6) (for the amplitude expansion). For the computational instances to be presented, the number of Chebyshev–Lobatto nodes $N = 401$ or 501 is adopted. For a few cases (where Re or E is large), higher resolutions up to $N = 1001$ will be used to get converged results.

4. Results and discussions

4.1. Validation of the numerical methods

To benchmark the present implementation of the numerical methods, we compare results from solving the linear eigenvalue problem (9) and evaluations of the various coefficients in (11) with those reported in Refs. [22,66], respectively. Good agreement has been achieved as detailed in Appendix B. Moreover, the Newtonian plane Poiseuille flow is taken as an example to illustrate the abilities of the saddle-point searching method and the linear CGLE method for the prediction of the AICI properties of the flow. Fig. 1 shows the variation of the linear growth rate with the frame moving speed v in this flow at $Re = 10000$, far from its linear critical condition of $Re_c = 5772.2218$. Overall, the two methods adopted in the present analysis produce consistent results. Comparatively, the result from the saddle-point searching method matches with the prediction in Ref. [49] better than that given by the linear CGLE, especially when v is away from that corresponding to the maximum linear growth rate. This is expected in that the linear CGLE is only a quadratic approximation of the true dispersion relation of the problem. The maximum linear growth rate, attained at about $v \approx 0.341$ is positive, indicating the linear instability of the flow. The leading-edge velocity of the wavepacket is $v_+ \approx 0.403$ and the trailing-edge velocity is $v_- \approx 0.288$. The positiveness of velocities suggests that the whole wavepacket moves in the same direction as the laminar base flow, and the disturbance cannot contaminate the upstream laminar flows. Therefore, the flow instability is of a convective nature, consistent with the conclusion of Ref. [49].

We would like to emphasise that the predictive ability of the AICI type by means of the linear CGLE is reliable, despite the minor deviation from the traditional method. In view of the shortcomings of the traditional method (see the discussions in Section 2), the linear CGLE method appears to be the only method with which we can conduct an extensive parametric study in a large parameter space.

4.2. Comparison of the two methods applying to the viscoelastic flows

We first present the AICI of the centre mode in the viscoelastic channel flow by locating saddle points in a complex wavenumber plane in a moving frame. As shown in Fig. 2, we take as an example the plane Poiseuille flow of Oldroyd-B fluids at $\beta = 0.8$, $E = 0.2$ and $Re = 500$. By solving the linear eigenvalue problem (9) at a given complex wavenumber α, one obtains the eigenspectrum of the complex phase speed c. In panel (a) of the figure, we plot three such eigenspectra for three different values of α. The case of the real-valued $\alpha = 1.0$ corresponds to the temporal stability analysis, and there is a single centre mode being linearly unstable (see the green cross above the horizontal line in the inset). For the complex wavenumbers $\alpha = 1.0 \pm 0.2i$, we also identify their centre modes (i.e., the red circle and blue dot in the inset). The linear growth rates μ_r corresponding to these three most unstable or least stable modes are represented by the three symbols in panel (b) where the contours of μ_r in the complex wavenumber plane α is shown. These results are obtained in the stationary frame of reference. In some flow systems, saddle points can be easily identified in the complex wavenumber plane; then the absolute growth rate of the disturbance can be evaluated at the saddle points and the AICI property is readily determined. However, for the present viscoelastic plane Poiseuille flow having centre-mode instabilities, the saddle point can be located far away from the real axis $\alpha_i = 0$, rendering the task of identifying the saddle point in the parameter space difficult (a circumstance similar to that encountered in Ref. [48]). The problem can be circumvented by locating saddle points in a moving frame as follows based on the method proposed by Deissler [49].

Recalling that the complex growth rate changes from $\mu(\alpha)$ in the laboratory frame to $\lambda(\alpha, v) = \mu(\alpha) + i\alpha v$ in a moving frame with velocity v, we plot in Fig. 2(c) the contours of λ_r in the same wavenumber plane but in a moving frame with $v = 1.0092$ (which value is the group velocity of the envelope of the whole wavepacket; when observing the wavepacket in the moving frame of this group velocity, the linear growth rate is the largest, see Fig. 2(f)). One can see that there appears a saddle point, marked by the yellow star, lying on the real axis $\alpha_i = 0$ and at the wavenumber $\alpha \approx 0.8618$ giving the largest growth rate. In the moving frame with the velocity $v = 1.005$, the saddle point moves below the real axis (see the green star in panel (d)). On the contrary, it moves above the real axis when a higher velocity $v = 1.013$ is used (the red star in panel (e)). In panels (c, d, e) we also superpose the locations (marked by black dots) of the corresponding saddle points predicted by the linear CGLE method (given by $(c_g - v)/(2ia_2) + \alpha_m$; see

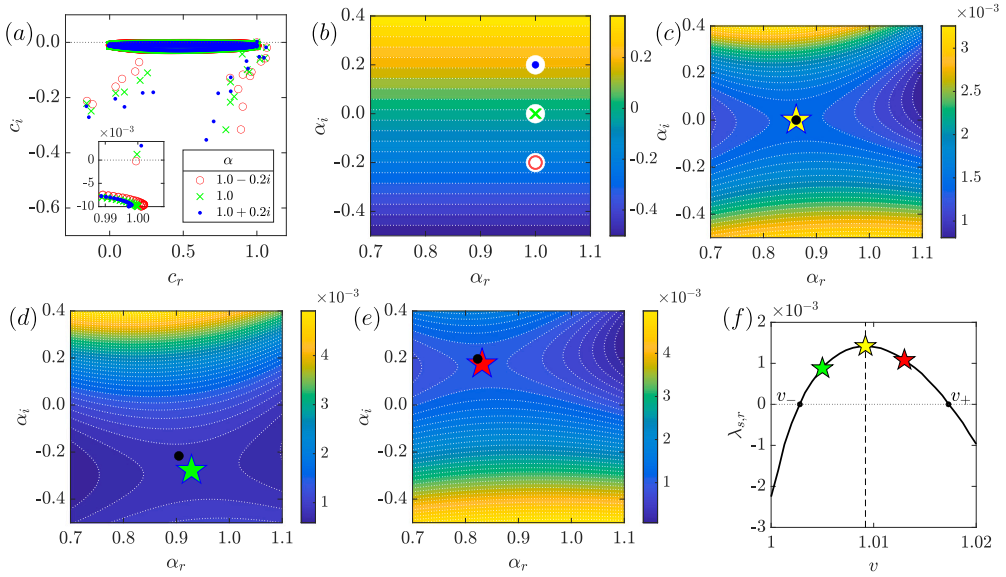

Fig. 2. Determination of the AICI property using the saddle-point searching method by locating saddles points in the complex wavenumber plane for the plane Poiseuille flow of Oldroyd-B fluids at $\beta = 0.8$, $E = 0.2$ and $Re = 500$. (*a*) Eigenspectra of the complex phase speed $c = c_r + ic_i$ for three different wavenumbers; the inset is an enlarged view around the corresponding most unstable or least stable modes. (*b*) Temporal linear growth rate μ_r in the complex wavenumber plane α in the laboratory frame ($v = 0$); the three circles correspond to the three most unstable or least stable modes in the inset of panel (*a*). (*c*) Spatio-temporal linear growth rate λ_r in the same complex wavenumber plane α but in a moving frame with velocity $v = 1.0092$; the star marks the saddle point. (*d*) λ_r in the moving frame with velocity $v = 1.005$. (*e*) λ_r in the moving frame with velocity $v = 1.013$. (*f*) The linear growth rate $\lambda_{s,r}$ at the saddle points observed in moving frames with varying velocity v; the three stars correspond to the three saddle points in panels (*c*), (*d*) and (*e*), respectively. Since the trailing-edge velocity $v_- > 0$, the flow instability is convective.

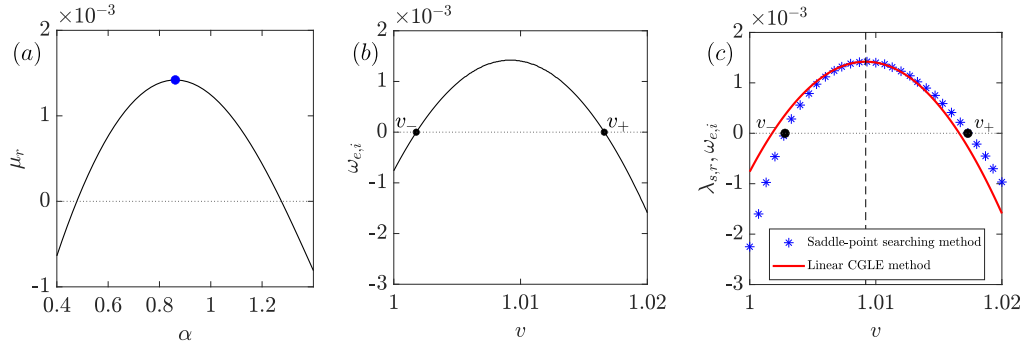

Fig. 3. Determination of the AICI property using the linear CGLE method for plane Poiseuille flow of Oldroyd-B fluids at $\beta = 0.8$, $E = 0.2$ and $Re = 500$. (*a*) The temporal linear growth rate μ_r as a function of the real-valued wavenumber α. (*b*) The spatio-temporal linear growth rate $\omega_{e,i}$ as a function of the frame-moving velocity v; the relation between $\omega_{e,i}$ and v is given in (15b). (*c*) Comparison of the results from the two methods: the obtained linear growth rate as a function of the frame moving velocity.

Eq. (14)). It can be seen that the prediction of the linear CGLE method is accurate when the saddle point is on the real axis $\alpha_i = 0$; however, the prediction becomes worse when the saddle point is further away from the axis. This is because the linear CGLE adopted is only a second-order approximation to the physical dispersion relation associated with the wavepacket dynamics [52]. In panel (*f*), the three accurate saddle points are also plotted as the three data points (marked by coloured stars accordingly) in the function curve $\lambda_{s,r} = \lambda_{s,r}(v)$ obtained by the saddle-point searching method. This curve can be obtained by tracing the saddle point in the complex wavenumber plane by varying the frame-moving speed v. The two roots satisfying $\lambda_{s,r}(v_-) = 0$ and $\lambda_{s,r}(v_+) = 0$ are marked in the panel by black dots, with $v_- \approx 1.0028$ corresponding to the trailing-edge velocity of the wavepacket and $v_+ \approx 1.0173$ the leading-edge velocity. An asymmetry of the curve about the group velocity 1.0092 (vertical dashed line) can be observed, similar to the situation in Newtonian plane Poiseuille flow [49]. The reason is not clear to us. Returning to the determination of AICI, since the trailing-edge velocity $v_- > 0$, the flow instability is convective.

The spatio-temporal instability of the flow can also be analysed using the linear CGLE method based on the amplitude expansion in a linear framework. For the case at $\beta = 0.8$, $E = 0.2$ and $Re = 500$, the variation of the linear growth rate μ_r with the real-valued wavenumber α is shown in Fig. 3(*a*) where the blue dot marks the wavenumber $\alpha_m \approx 0.8618$ producing the largest linear growth rate $\mu_r = 0.00142$. Evaluation of the coefficients in (11) at this wavenumber α_m gives $a_1 = 0.001420 - 0.860354i$, $c_g = 1.009197 - 0.000002i$ and $a_2 = 0.009330 - 0.001849i$. Then the linear growth rate as a function of the frame-moving velocity $\omega_{e,i} = \omega_{e,i}(v)$ described in (15b) can be plotted as shown in panel (*b*) (note the symmetry of the predicted curve, different from the former saddle-point searching method; the symmetry stems naturally from the second-order approximation as in (14), so the function $\omega_{e,i} = \omega_{e,i}(v)$ is parabolic). Since the trailing-edge velocity of the wavepacket evaluated ($v_- \approx 1.0018$) is positive, the linear CGLE method predicts convective instability for the flow.

In the above, two different methods are adopted to determine the AICI property of the viscoelastic channel flow, with each method generating a plot of the spatio-temporal linear growth rate as a function of the frame-moving velocity. Fig. 3(*c*) shows a comparison of results from these two methods by superposing Fig. 2(*f*) and Fig. 3(*b*) (note that we have used different notations $\lambda_{s,r}$ and $\omega_{e,i}$ for the growth rate

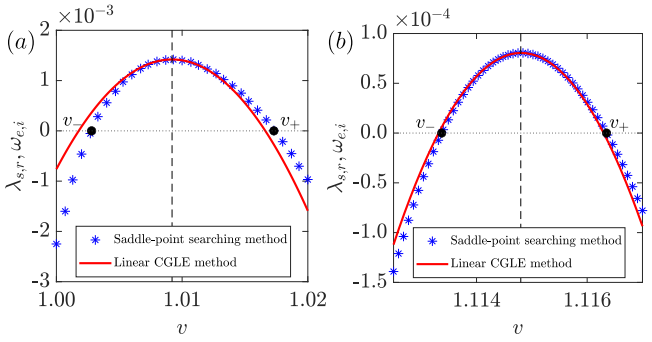

Fig. 4. Comparison of the predicted spatio-temporal linear growth rates from the saddle-point searching method and the linear CGLE method for the viscoelastic plane Poiseuille flow at $\beta = 0.8$, $E = 0.2$ and $Re = 500$ based on the FENE-P fluid model with a maximum polymer extensibility of $L = 200$ (a) and $L = 100$ (b), respectively. The linear instability pertains to a centre mode.

to distinguish the two methods). Overall, the agreement is favourable, especially in the range of υ where the growth rate is positive. Regarding the trailing-edge velocity υ_-, the linear CGLE predicts $\upsilon_- \approx 1.0018$, which deviates slightly from the value of $\upsilon_- \approx 1.0028$ predicted by the saddle-point searching method, with the relative error being about 0.1%.

In addition to the Oldroyd-B fluid model, we have also compared the corresponding predictions using the FENE-P fluid model as shown in Figs. 4(a, b) (for maximum polymer extensibility $L = 200$ and 100, respectively). Results from the linear CGLE method and the saddle-point searching method show a quantitative agreement. The trailing-edge velocities in the two cases are all $\upsilon_- \approx 1 > 0$, indicating the convective nature of the centre-mode instability for viscoelastic channel flows of FENE-P fluids. Moreover, the finite polymer extensibility seems to reduce the degree of asymmetry of the curves in these plots. Same as that for the Oldroyd-B model, the linear CGLE method slightly underestimates the trailing-edge velocity υ_- predicted by the saddle-point searching method. In the following, we continue to use the linear CGLE method in the parametric study of the spatio-temporal instability of the centre mode.

4.3. A parametric study of AICI of the centre mode

Fig. 5(a) shows the contours of the linear growth rate in a Re–α plane for the flow at $\beta = 0.8$ and $E = 0.2$ based on the Oldroyd-B fluid model, where the solid curve is the neutral curve. The calculation of the coefficients in the linear CGLE is performed at the wavenumber α_m at which the linear growth rate is maximised for each Re (that is, the red dashed line starting from the linear critical condition marked by the red star traces the variation of α_m with Re). Based on the obtained coefficients, the wavepacket velocities υ_-, c_g and υ_+ around the parametric point $(\beta, E, Re) = (0.8, 0.2, 1000)$ are calculated and plotted in the remaining panels of Fig. 5. Panel (b) shows the effect of Re at $(\beta, E) = (0.8, 0.2)$. The linear critical Reynolds number is about 169, marked by the red star in the panel. Upon increasing Re, the flow becomes linearly unstable. The velocities of the trailing edge and the leading edge of the wavepackets are about one, indicating also the convective instability of the flow ($\upsilon_- > 0$). Far from the linear critical condition, the wavepacket velocities are almost independent of Re. In panel (c) the elasticity number E is varied and the other parameters are fixed at $(\beta, Re) = (0.8, 1000)$. The group velocity c_g increases with E, while the variations of υ_+ and υ_- are not monotonic. Nevertheless, they are much larger than zero, suggestive of again the convective instability. The effect of varying β with fixed values of $(E, Re) = (0.2, 1000)$ is illustrated in panel (d). The overall trend is that c_g decreases monotonically with increasing β, whereas υ_+, υ_- decrease but non-monotonically (note that the centre-mode instability ceases to exist for $\beta \lesssim 0.5$ as first reported in Ref. [22]). As the value of υ_- is about one, the instability is still convective in the range of β investigated. From the above results, we can observe the persistent convective instability of the viscoelastic channel flow in the parameter space around the parametric point $(\beta, E, Re) = (0.8, 0.2, 1000)$.

Further exploration of the spatio-temporal instability in a large parameter space covering approximately $\beta \in (0.65, 0.95)$, $E \in (0.05, 1.6)$ and $Re \in (0, 2000)$ shows that the trailing-edge velocity υ_- corresponding to the centre-mode instability in the flow of Oldroyd-B fluids is always close to one as plotted in Fig. 6(a), implying that the instability is convective. In addition to these observations based on the Oldroyd-B fluid model, we present in panel (b) the corresponding variations of υ_- using the FENE-P fluid model with a maximum polymer extensibility of $L = 200$. For the high polymer concentration of $\beta = 0.65$, the centre-mode instability ceases to exist within the Re explored (thus no blue curves in panel (b)). When $\beta = 0.8$ and $E = (0.2, 0.4)$, the centre-mode instability only exists in a certain range of Re (confined by the red dots and squares). These results indicate the stabilising effect of the FENE-P model on the centre-mode instability, consistent with that reported in Ref. [25] for the centre mode in viscoelastic pipe flows. For dilute polymer solutions of $\beta = (0.9, 0.95)$ the instability persists for the FENE-P fluid model. Moreover, regarding the value of the trailing-edge velocity, it can be seen that υ_- increases for all the FENE-P fluids compared to the Oldroyd-B model as long as the flow is linearly unstable. Such an increase in υ_- suggests that the instability in viscoelastic channel flow of FENE-P fluids is "more convective" than that of the Oldroyd-B fluids. The effect of varying L on the AICI will be further investigated below in Section 4.5.

4.4. High-Re behaviour of the centre-mode AICI

We observe in the last section that the characteristic velocities υ_+, c_g and υ_- of the centre-mode instability approach constants at high Re (see Figs. 5(b) and 6(a)) for a given parameter setting (β, E). This tempts one to look into the asymptotical spatio-temporal behaviour of the centre mode at high Re. Deissler [49] have conducted an asymptotic analysis of the Newtonian channel flows at high Re, which however pertains to the wall mode. Linear and nonlinear scaling laws exist in the high-Re limit of the viscoelastic centre mode [21,22,26,27]. As the centre-mode instability persists down to very small $Re \approx 5$, we consider cases at $Re = O(1000)$ as high-Re scenarios. In the following, we will first show numerical results of the scaling behaviour of the large-Re centre mode and then provide our theoretical derivation of the same scaling.

Fig. 7 illustrates the compensated variables as a function of Re. Especially, the compensated variables (for α_m, a_1, c_g, a_2, υ_s) approach constant at large Re, indicating the asymptotic behaviour of these variables, to be discussed as follows.

- Panel (a) shows the value of the wavenumber α_m (scaled by $E^2 Re$; at α_m the linear growth rate is maximised). One can see that at each β the curves for different E collapse onto a single horizontal line at large Re, implying $\alpha_m E^2 Re$ becomes independent of Re and E at a given β, i.e., α_m scales with $E^{-2} Re^{-1}$.
- Panel (b) plots the corresponding variation of the maximum linear growth rate a_{1r} (scaled by ERe). For each β we probed three different values of E consisting of a low, an intermediate and a high value. For the quantity a_{1r}, only the curves for the low and intermediate values of E can collapse up to $Re = 2000$. Similarly, Khalid et al. [22] found that the neutral curves for the centre-mode instability in the same flow can only collapse for low values of E at a given β (see Figure 11 therein). Nevertheless, all the curves in panel (b) seem to become horizontal at high Re (except those for $\beta = 0.65$ which would require higher Re to manifest the trend), implying the scaling law of $a_{1r} \propto E^{-1} Re^{-1}$ at relatively small E.

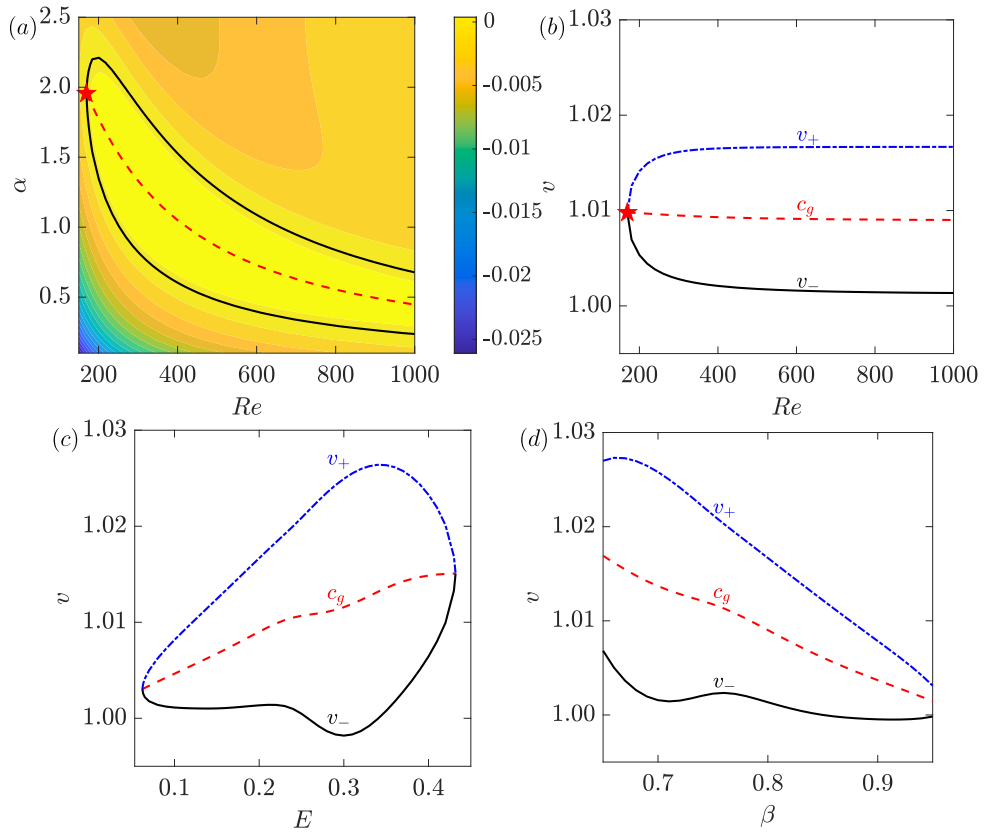

Fig. 5. (*a*) Contours of the linear growth rate in a Re–α plane for the flow of Oldroyd-B fluids at $\beta = 0.8$ and $E = 0.2$. The solid curve is the neutral curve with the red star marking its linear critical condition. The dashed curve traces the wavenumber α_m. The corresponding characteristic velocities of the wavepackets (all obtained using the linear CGLE method): (*b*) at varying Re for $\beta = 0.8$ and $E = 0.2$; (*c*) at varying E for $\beta = 0.8$ and $Re = 1000$; (*d*) at varying β for $E = 0.2$ and $Re = 1000$. c_g, v_- and v_+ are the group velocity, wave trailing-edge velocity and wave leading-edge velocity, respectively.

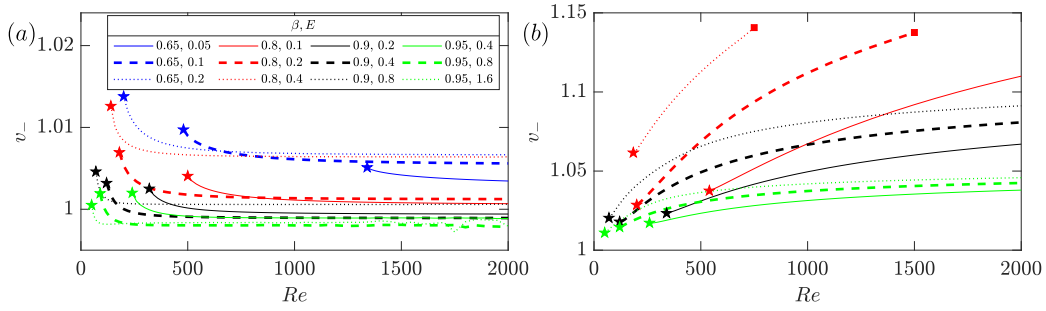

Fig. 6. Trailing-edge velocity v_- of the wavepacket in viscoelastic channel flows at varying Re for different combinations of β and E based on: (*a*) the Oldroyd-B fluid model; (*b*) the FENE-P fluid model with a maximum polymer extensibility of $L = 200$. The linear instability pertains to the centre mode. The stars and squares mark approximately the beginning (as that in Fig. 5(*b*)) and ending respectively of the centre-mode instability upon increasing Re.

- Panels (c, d) show the variations of the scaled a_{2r} and a_{2i} (the real and imaginary parts of the diffusion coefficient a_2). Since a_{2i} is always negative, we add to it a negative sign in the log scale. From these two panels, we observe the scaling behaviours of $a_{2r} \propto E^3 Re$ and $a_{2i} \propto E^3 Re$ for each given β. The wiggles for $\beta = 0.95$ curves are due to its high resolution requirement, even though we have used $N = 1001$ Chebyshev–Lobatto nodes in this case.
- Panels (e, f) display the high-Re results of the group velocity c_g and the wave spreading rate $v_s \equiv v_+ - v_-$, respectively. Like the trend present in panel (*b*), the collapse of curves only happens for relatively low E, implying the scalings of $(c_g - 1) \propto E$ and $v_s \propto E$ at a given β, and specifically for $\beta = 0.65$ higher Re would be required to exhibit the scaling.

These scaling laws are summarised as

$$\alpha_m \propto E^{-2} Re^{-1}, \quad a_{1r} \propto E^{-1} Re^{-1}, \quad a_{2r} \propto E^3 Re, \tag{18a,b,c}$$

$$a_{2i} \propto E^3 Re, \quad (c_g - 1) \propto E, \quad v_s \propto E. \tag{18d,e,f}$$

Since they are valid for each given β, they can be re-written in the forms of

$$\alpha_m = f_1(\beta) E^{-2} Re^{-1}, \quad a_{1r} = f_2(\beta) E^{-1} Re^{-1}, \quad a_{2r} = f_3(\beta) E^3 Re, \tag{19a,b,c}$$

$$a_{2i} = f_4(\beta) E^3 Re, \quad c_g = 1 + f_5(\beta) E, \quad v_s = f_6(\beta) E, \tag{19d,e,f}$$

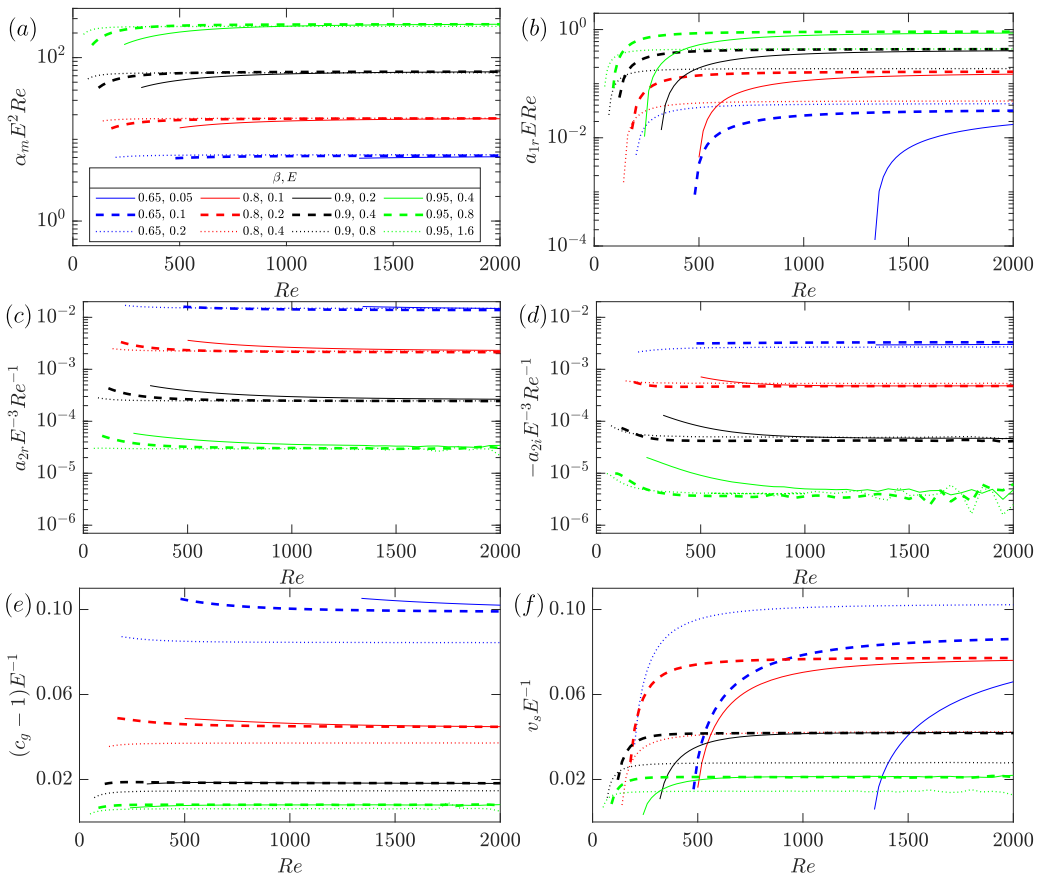

Fig. 7. Scaling laws of various quantities in the determination of the centre-mode AICI in plane Poiseuille flow based on the Oldroyd-B fluid model. (a) The wavenumber α_m at which the linear growth rate a_{1r} is maximised; $\alpha_m E^2 Re \to$ Const. at high Re and the collapse of curves for different E implies the scaling law of $\alpha_m \propto E^{-2} Re^{-1}$ at a given viscosity ratio β. (b) The maximum linear growth rate a_{1r} corresponding to the α_m in panel (a). (c, d) The real part a_{2r} and imaginary part a_{2i} of the diffusion coefficient a_2. (e) The group velocity c_g. (f) The spreading rate of the wavepacket v_s.

where $f(\beta)$s with subscripts represent coefficients which are functions of β only. Next, we will use an asymptotic approach to theoretically derive these numerically observed scaling laws. Since the present work is primarily dedicated to the determination of AICI of the flow, we only present the gist of the asymptotic approach. More details of the approach for viscoelastic pipe flows has been presented in Ref. [26], where a three-layered asymptotic model consisting of a viscous wall-layer, a main layer and a viscoelastic centre layer was analysed.

The flow regime of interest in the determination of AICI of the flow is at high Re for the viscosity ratio within $0.65 \lesssim \beta \lesssim 0.95$, an intermediate level of polymer concentration. The centre-mode instability at large Re is associated with a small wavenumber α (taken to be a real number here), i.e., the centre mode is of a long-wavelength nature. For $0.65 \lesssim \beta \lesssim 0.95$, we follow the asymptotic analysis of the long wave-length centre mode for an intermediate level of concentration in Ref. [26]

$$Re \gg 1, \quad Re^{-1} \ll \alpha \ll 1, \quad (\beta, 1-\beta) = O(1). \tag{20a,b,c}$$

Besides, the balance of various terms in the governing Eqs. (5) in the spectral space when $L \to \infty$ (Oldroyd-B model) shows that the elastic and viscous centre layers scale as, respectively, $y = O(\alpha^{-1/2} Wi^{-1/2})$ and $y = O(\alpha^{-1/4} Re^{-1/4})$. As pointed out by Dong & Zhang [26], it is the balance of these two layers that induces the centre-mode linear instability (see their Section 3.1), leading to the relation

$$Wi \sim \alpha^{-1/2} Re^{1/2}. \tag{21}$$

In order to take into account this relation, scaled Re and Wi are introduced as

$$R_1 = Re/\beta, \quad W_1 = \alpha^{1/2} R_1^{-1/2} Wi. \tag{22a,b}$$

Especially, $W_1 = O(1)$ despite the values of α, R_1 or Wi at a given $\beta \in [0.65, 0.95]$. Moreover, the complex phase speed c (note that $\mu = -i\alpha c$) can be approximately expressed as

$$c = 1 + \alpha^{-1/2} R_1^{-1/2} c_1. \tag{23}$$

Here c_1 is also of order 1 for the β considered [26].

By inserting (22a) into (22b), one can express the wavenumber as

$$\alpha = W_1^2 \beta^{-1} Re Wi^{-2} = W_1^2 \beta^{-1} E^{-2} Re^{-1}. \tag{24}$$

Then one can see that for a given parameter setting of (β, E, Re) the wavenumber α_m at which the maximum linear growth rate is attained corresponds to a proper value of W_1 (we denote this value as W_{1m} with the associated c_1 having a real part of $c_{1r,m}$ and an imaginary part of $c_{1i,m}$). As W_{1m} only depends on β, we may describe α_m as

$$\alpha_m = W_{1m}^2 \beta^{-1} E^{-2} Re^{-1} = f_1(\beta) E^{-2} Re^{-1}, \tag{25}$$

i.e., the scaling law observed numerically in (19a). From (23) the real and imaginary parts of c are

$$c_r = 1 + \alpha^{-1/2} \beta^{1/2} Re^{-1/2} c_{1r}, \quad c_i = \alpha^{-1/2} \beta^{1/2} Re^{-1/2} c_{1i}. \tag{26}$$

Then the real and imaginary parts of the complex growth rate $\mu = -i\alpha c$ are

$$\mu_r = \alpha c_i = \alpha^{1/2} \beta^{1/2} Re^{-1/2} c_{1i}, \quad \mu_i = -\alpha c_r = -\alpha - \alpha^{1/2} \beta^{1/2} Re^{-1/2} c_{1r}. \tag{27a,b}$$

The maximum linear growth rate a_{1r} can be obtained from μ_r at α_m corresponding to W_{1m} (and thus $c_{1i,m}$ is attained) as

$$a_{1r} = \mu_r(\alpha_m, c_{1i,m}) = [f_1(\beta)]^{1/2} \beta^{1/2} E^{-1} Re^{-1} c_{1i,m} = f_2(\beta) E^{-1} Re^{-1}, \tag{28}$$

which is the scaling law observed numerically in (19b).

In terms of the diffusion coefficient a_2, noting that it can be approximately evaluated from the dispersion relation (12c), one then obtains from (27) the expressions of a_{2r} and a_{2i} evaluated at the wavenumber α_m which corresponds to W_{1m} and $c_{1r,m}+ic_{1i,m}$ as (note that the chain rule $\frac{d}{d\alpha}=\frac{d}{dW_1}\frac{dW_1}{d\alpha}$ needs to be used for c_{1r} and c_{1i})

$$a_{2r}\approx-\frac{1}{2}\frac{\partial^2\mu_r}{\partial\alpha^2}\bigg|_{\alpha_m,W_{1m}}=\frac{1}{8}\left(\frac{c_{1i}}{W_1^3}-\frac{1}{W_1^2}\frac{dc_{1i}}{dW_1}-\frac{1}{W_1}\frac{d^2c_{1i}}{dW_1^2}\right)\bigg|_{W_{1m}}\beta^2E^3Re$$
$$=f_3(\beta)E^3Re, \tag{29a}$$

$$a_{2i}\approx-\frac{1}{2}\frac{\partial^2\mu_i}{\partial\alpha^2}\bigg|_{\alpha_m,W_{1m}}=-\frac{1}{8}\left(\frac{c_{1r}}{W_1^3}-\frac{1}{W_1^2}\frac{dc_{1r}}{dW_1}-\frac{1}{W_1}\frac{d^2c_{1r}}{dW_1^2}\right)\bigg|_{W_{1m}}\beta^2E^3Re$$
$$=f_4(\beta)E^3Re, \tag{29b}$$

where $f_3(\beta)$ and $f_4(\beta)$ are only functions of β. These are consistent with the scaling laws (19c,d). As for the group velocity c_g, it can also be evaluated from the dispersion relation (12a) as

$$c_g\approx-\frac{\partial\mu_i}{\partial\alpha}\bigg|_{\alpha_m,W_{1m}}=1+\frac{1}{2}\left(\frac{c_{1r}}{W_1}+\frac{dc_{1r}}{dW_1}\right)\bigg|_{W_{1m}}\beta E=1+f_5(\beta)E, \tag{30}$$

which is consistent with the scaling (19e). Lastly, for the spreading rate v_s, we have

$$v_s\equiv v_+-v_-$$
$$=2\sqrt{\frac{4|a_2|^2a_{1r}}{a_{2r}}}=2\sqrt{\frac{4[f_3^2(\beta)E^6Re^2+f_4^2(\beta)E^6Re^2]f_2(\beta)E^{-1}Re^{-1}}{f_3(\beta)E^3Re}}$$
$$=4\sqrt{\frac{[f_3^2(\beta)+f_4^2(\beta)]f_2(\beta)}{f_3(\beta)}}E=f_6(\beta)E, \tag{31}$$

being in agreement with the scaling (19f).

The above theoretical derivations support the scaling laws observed numerically as summarised in (19). From these scalings, one can see that the wavenumber α_m and the maximum linear growth rate a_{1r} decrease with Re, while for the diffusion coefficient a_2 its real and imaginary parts a_{2r} and a_{2i} increase with Re; this suggests that at high Re the wavepacket grows more slowly but diffuses faster, with the combined effect to make the wavepacket spread at a constant speed of v_s. In the determination of AICI of the flow, the trailing-edge velocity v_- plays the decisive role. Since $v_-=c_g-v_s/2$ (as can be seen from (16a) and (17)), for a given (β,E) the asymptotic values of c_g and v_s at high Re imply an asymptotic value of v_-, that is,

$$v_-=c_g-\frac{v_s}{2}\approx c_g-\frac{c_g-1}{2}=\frac{c_g+1}{2}\approx1, \tag{32}$$

where we have used the approximation $v_s\approx c_g-1$ as numerically observed from Fig. 7(e,f), and the fact that the group velocity $c_g\approx1$ for the centre-mode instability. This indicates the convective instability of the centre mode in viscoelastic channel flows at asymptotically large Re.

4.5. Effects of finite extensibility of polymers on the centre mode

In this section, we examine how the finite polymer extensibility L affects the spatio-temporal instability of the centre mode in the viscoelastic channel flow. Figs. 8(a) and (b) show the neutral curves (solid curves) and the characteristic wave velocities, respectively, at various L, $\beta=0.8$ and $E=0.2$. The results for $L=\infty$ are the same as those presented in Fig. 5(a,b) for the Oldroyd-B model. Bringing L down from infinity to a finite value of 10000 exerts no visible effect on both the neutral curve or the wavepacket velocities (the black and cyan curves coincide). After further reducing the extensibility to $L=1000$, the neutral curve still shows no apparent deviation, while all three wavepacket velocities v_-,c_g,v_+ increase, especially when Re is large (the right part of the red curves bending up), with the largest increase happening at the highest Re investigated. When $L=200$, the neutral curve shrinks and the wavepacket velocities increase further. For the lowest extensibility explored $L=100$, the neutral curve takes the form of a closed loop, which continues to shrink with L further decreased; meanwhile, the wavepacket velocities are the highest. The centre-mode instability disappears when the polymer extensibility is further reduced. In addition, the spreading rate of the wavepacket $v_s\equiv v_+-v_-$ is reduced when the extensibility becomes smaller. These results suggest that as long as the centre-mode instability exists, the finite polymer extensibility makes the whole disturbance wavepacket travel faster downstream.

5. Conclusions

In this paper, the spatio-temporal instability of viscoelastic plane Poiseuille flows (modelled with the Oldroyd-B and FENE-P models) subjected to infinitesimally small disturbances has been investigated in a linear framework. The focus of our work is to determine the convective or absolute nature of the centre mode in these flows. The main approach adopted for the determination of the AICI property is based on a linear complex Ginzburg–Landau equation (CGLE) which governs the spatio-temporal evolution of infinitesimal disturbances, favoured by its relatively cheap computational burden and wider applicability in the parametric space, compared to the conventional saddle-point searching method. Several comparative examples demonstrate the good agreement of characteristic wavepacket velocities predicted by the two approaches, all indicating the convective nature of the flow instability of the novel centre mode recently discovered by Khalid et al. [22] in this flow.

Extensive parametric studies have then been conducted using the Oldroyd-B fluid model, confirming the persistent convective nature of the centre-mode linear instability of the viscoelastic channel flow in a large parameter space. Specifically, the trailing-edge velocity v_- has been evaluated at parameters in the range of $0.65\le\beta\le0.95$, $0.05\le E\le1.6$ and $0\le Re\le2000$. The results show that starting from the linear critical Reynolds numbers, v_- first decreases and then becomes independent of Re in all cases. The values of v_- are all close to one, even at asymptotically large Re, indicating clearly that the centre-mode instability is convective. This trend at high Re is supported by an asymptotic analysis following the method in Dong & Zhang [26]. The theoretical analysis also explains the scaling laws of some compensated quantities that we have observed numerically.

As a distinguished feature in the present viscoelastic rectilinear flow, absolute instability is missing even at parameters exhibiting highly strong polymer elasticity. This suggests that other complex mechanisms must play a role in making the linear instability absolute in the viscoelastic jets, mixing layers, mixed convection flows, and flows over a confined cylinder [34,35,38,39]. The physical reason for the present convective instability stems from the relatively high phase speed, low growth rate and low spreading rate of the unstable centre modes, all preventing them from travelling upstream (as in formulae (16a)). This work can be extended in several ways. For example, three-dimensional flows could be analysed to depict more closely the flow structures in the wave evolution. A more interesting future direction lies in the comparison to experimental work. The recent experiment by Shnapp & Steinberg [20] on the spatio-temporal development of the disturbance in viscoelastic channel flows at vanishingly small Re was conducted in a highly nonlinear regime. Their elastic pulse-splitting phenomenon is thus likely due to the nonlinear effect, negating a direct comparison of our results to theirs. Future work can consider either conducting a nonlinear AICI analysis [67] from the theoretical perspective or purposely investigating the linear development in the experiments, to which our results may be of some help.

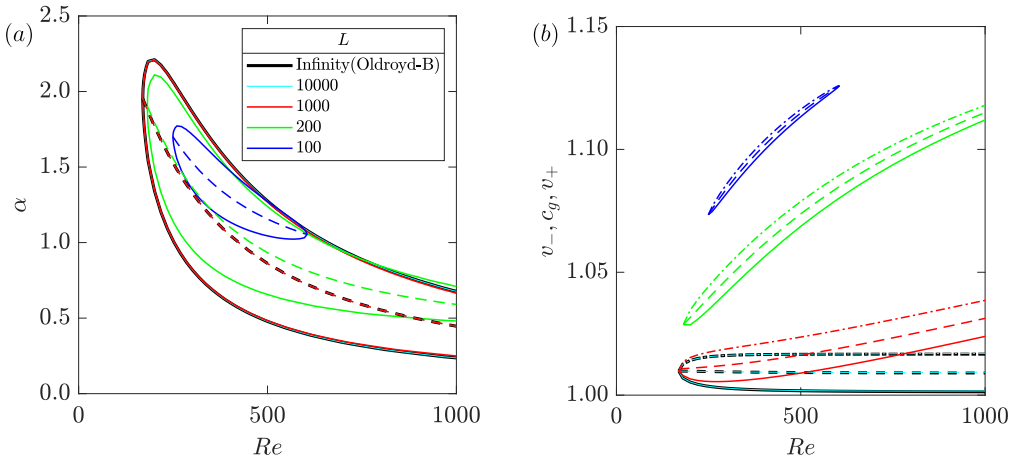

Fig. 8. Spatio-temporal instabilities in plane Poiseuille flow of FENE-P fluids at $\beta = 0.8$ and $E = 0.2$. (*a*) The gradual shrink of the neutral curves with decreasing the finite extensibility of polymers L (the flow is linearly unstable within the curves and the linear growth rate is maximised along the dashed lines). (*b*) The characteristic velocities of the wavepackets corresponding to the cases in panel (*a*): solid for v_-, dashed for c_g and dot-dashed for v_+.

Declaration of competing interest

The authors declare that they have no known competing financial interests or personal relationships that could have appeared to influence the work reported in this paper.

Data availability

Data will be made available on request.

Acknowledgements

DW is supported by a PhD scholarship (No. 201906220200) from the China Scholarship Council and the NUS research scholarship. MZ acknowledges the financial support of NUS (Suzhou) Research Institute and National Natural Science Foundation of China (Grant No. 12202300). DX is supported by the National Natural Science Foundation of China (No. 92152106). The HPC@NUS IT is acknowledged for providing the computational resources.

Appendix A. Calculation of the coefficients in the linear CGLE

We express the disturbance $\boldsymbol{\gamma}$ in the amplitude expansion as

$$\boldsymbol{\gamma} = \left(A\tilde{\boldsymbol{\gamma}}_{11}e^{i\alpha x} + \text{c.c.}\right) + \left(\frac{\partial A}{\partial x}\tilde{\boldsymbol{\gamma}}_{21}e^{i\alpha x} + \text{c.c.}\right) + \left(\frac{\partial^2 A}{\partial x^2}\tilde{\boldsymbol{\gamma}}_{31}e^{i\alpha x} + \text{c.c.}\right) + \cdots, \tag{A.1}$$

where $A = A(x,t)$ is the disturbance amplitude, $\tilde{\boldsymbol{\gamma}}$ with subscripts are wave shape functions, and the wavenumber α is taken to be real-valued in this method. The linear CGLE (11) is copied below for convenience

$$\frac{\partial A}{\partial t} = -c_g\frac{\partial A}{\partial x} + a_1 A + a_2\frac{\partial^2 A}{\partial x^2}. \tag{A.2}$$

Inserting (A.1) and (A.2) into (7) and collecting like terms with the same amplitude result in a series of equations to be solved

$$(a_1\widetilde{\boldsymbol{M}} - \widetilde{\boldsymbol{L}}_1)\tilde{\boldsymbol{\gamma}}_{11} = \boldsymbol{0}, \tag{A.3a}$$

$$(a_1\widetilde{\boldsymbol{M}} - \widetilde{\boldsymbol{L}}_1)\tilde{\boldsymbol{\gamma}}_{21} = c_g\widetilde{\boldsymbol{M}}\tilde{\boldsymbol{\gamma}}_{11} + \tilde{\boldsymbol{n}}_{21} \text{ with } \tilde{\boldsymbol{n}}_{21} = \widetilde{\boldsymbol{L}}_1^{\circ}\tilde{\boldsymbol{\gamma}}_{11} \tag{A.3b}$$

$$(a_1\widetilde{\boldsymbol{M}} - \widetilde{\boldsymbol{L}}_1)\tilde{\boldsymbol{\gamma}}_{31} = -a_2\widetilde{\boldsymbol{M}}\tilde{\boldsymbol{\gamma}}_{11} + \tilde{\boldsymbol{n}}_{31} \text{ with } \tilde{\boldsymbol{n}}_{31} = \widetilde{\boldsymbol{L}}_2^{\circ}\tilde{\boldsymbol{\gamma}}_{11} + (\widetilde{\boldsymbol{L}}_1^{\circ} + c_g\widetilde{\boldsymbol{M}})\tilde{\boldsymbol{\gamma}}_{21}. \tag{A.3c}$$

Following Ref. [53] (which in turn followed the solution strategy originally proposed by [68] and refined recently by [61]), we apply an orthogonality condition to make the coefficients c_g and a_2 uniquely determined. The condition requires the projection of an eigenfunction $\tilde{\boldsymbol{f}}$ onto the eigenfunction $\tilde{\boldsymbol{\gamma}}_{11}$ of the first harmonic to be zero

$$\langle\tilde{\boldsymbol{\gamma}}_{11}, \tilde{\boldsymbol{f}}\rangle_{\mathcal{M}} \equiv \tilde{\boldsymbol{\gamma}}_{11}^{\mathrm{H}}\mathcal{M}\tilde{\boldsymbol{f}} = 0, \tag{A.4}$$

where the superscript $^{\mathrm{H}}$ means conjugate transpose and $\mathcal{M}$ is a positive definite Hermitian matrix (set to be the identity matrix in the present analysis). Applying the condition (A.4) to $\tilde{\boldsymbol{f}} = \tilde{\boldsymbol{\gamma}}_{21}$ and $\tilde{\boldsymbol{\gamma}}_{31}$ gives

$$\tilde{\boldsymbol{\gamma}}_{11}^{\mathrm{H}}\mathcal{M}\tilde{\boldsymbol{\gamma}}_{21} = 0, \qquad \tilde{\boldsymbol{\gamma}}_{11}^{\mathrm{H}}\mathcal{M}\tilde{\boldsymbol{\gamma}}_{31} = 0. \tag{A.5}$$

Then, the augmentation of (A.3b) and (A.3c) with (A.5) results in two extended equation systems

$$\begin{bmatrix}(a_1\widetilde{\boldsymbol{M}} - \widetilde{\boldsymbol{L}}_1) & -\widetilde{\boldsymbol{M}}\tilde{\boldsymbol{\gamma}}_{11}\\ \tilde{\boldsymbol{\gamma}}_{11}^{\mathrm{H}}\mathcal{M} & 0\end{bmatrix}\begin{bmatrix}\tilde{\boldsymbol{\gamma}}_{21}\\ c_g\end{bmatrix} = \begin{bmatrix}\tilde{\boldsymbol{n}}_{21}\\ 0\end{bmatrix}, \begin{bmatrix}(a_1\widetilde{\boldsymbol{M}} - \widetilde{\boldsymbol{L}}_1) & \widetilde{\boldsymbol{M}}\tilde{\boldsymbol{\gamma}}_{11}\\ \tilde{\boldsymbol{\gamma}}_{11}^{\mathrm{H}}\mathcal{M} & 0\end{bmatrix}\begin{bmatrix}\tilde{\boldsymbol{\gamma}}_{31}\\ a_2\end{bmatrix} = \begin{bmatrix}\tilde{\boldsymbol{n}}_{31}\\ 0\end{bmatrix}. \tag{A.6}$$

Solving these two equation systems and Eq. (A.3a) results in the coefficients in the linear CGLE (11) in the main text.

Appendix B. Validation of the adopted methods

Solving the linear eigenvalue problem (9) accurately is the essential part of locating the saddle point for the determination of AICI. We validate the present code by comparing the obtained complex phase speeds c with those reported by Khalid et al. [22]. The results listed in Table B.1 correspond to the unstable mode at given parameter settings. A good agreement can be observed in all three cases, including both wall-mode instability and centre-mode instability.

Additionally, calculations of the coefficients of the linear CGLE are shown in Table B.2 for a Newtonian channel flow at its linear critical condition. The results obtained from the amplitude expansion (11) and those evaluated using the dispersion relation (12) agree well with each other. In the same table, we also list the corresponding results of multiple-scale expansion reported by Zhang [66] for the validation. A favourable agreement has been achieved for both the group velocity c_g and the coefficient a_2. The definition of a_1 in the multiple-scale expansion of Ref. [66] is related to the present one by the transformation $\bar{a}_1 \equiv (\partial a_1/\partial Re)|_{Re_c}$. It should be noted that the dispersion relation (12) only gives an approximation of the coefficients in the linear CGLE (11).

Table B.1
Validation of the complex phase speed c of the unstable mode in 2-D viscoelastic channel flow of Oldroyd-B fluids.

Mode type	β, E, Re, α	Results in Ref. [22]	The present
wall mode	0.5, 0.001, 3960, 1.15	$0.29643 + 1.73 \times 10^{-7} i$	$0.2964299 + 1.7294 \times 10^{-7} i$
centre mode	0.96, 0.9, 650, 1	$1.00087623 + 0.00130115 i$	$1.0008762331 + 0.0013011542 i$
centre mode	0.6, 0.1, 800, 0.6	$0.99778 + 5.78112 \times 10^{-5} i$	$0.9977842 + 5.7811180 \times 10^{-5} i$

Table B.2
Validation of the coefficients in the linear CGLE for a 2-D Newtonian channel flow at its linear critical condition $Re_c = 5772.2218$ and $\alpha_c = 1.0205474$. Note that there is a sign difference of c_g between the study in Ref. [66] and the present. The coefficient a_1 in their study, obtained from a multiple-scale expansion, is equivalent to $\tilde{a}_1 \equiv (\partial a_1/\partial Re)|_{Re_c}$ in the present amplitude expansion. The last column shows the evaluations of the coefficients based on the linear dispersion relation (12).

	Results in Ref. [66]	The present (using (11))	The present (using (12))
c_g	$-0.3830990 - 0.0000000 i$	$0.383098803 + 0.000000019 i$	$0.383098802 + 0.000000018 i$
a_1	–	$-0.000000000 - 0.269424774 i$	$-0.000000000 - 0.269424774 i$
$\tilde{a}_1$	$(1.6825 + 8.1128 i) \times 10^{-6}$	$(1.6821 + 8.1120 i) \times 10^{-6}$	$(1.6821 + 8.1120 i) \times 10^{-6}$
a_2	$0.1867144 + 0.0274815 i$	$0.186714427 + 0.027481516 i$	$0.186714926 + 0.027481752 i$

References

[1] B.A. Toms, Some observations of the flow of linear polymer solution through straight tubes at large Reynolds numbers, in: Proceedings of the First International Congress on Rheology, North-Holland, Amsterdam, 1949.
[2] P.S. Virk, Drag reduction fundamentals, AIChE J. 21 (4) (1975) 625–656.
[3] E.D. Burger, W.R. Munk, H.A. Wahl, Flow increase in the trans alaska pipeline through use of a polymeric drag-reducing additive, J. Pet. Technol. 34 (02) (1982) 377–386.
[4] R. Sellin, M. Ollis, Polymer drag reduction in large pipes and sewers: Results of recent field trials, J. Rheol. 24 (5) (1980) 667–684.
[5] National Research Council, Technology for the United States Navy and Marine Corps, 2000-2035: Becoming a 21st-Century Force, Vol. 6, The National Academies Press, 1997.
[6] C.M. White, M.G. Mungal, Mechanics and prediction of turbulent drag reduction with polymer additives, Annu. Rev. Fluid Mech. 40 (1) (2008) 235–256.
[7] M.D. Graham, Drag reduction and the dynamics of turbulence in simple and complex fluids, Phys. Fluids 26 (10) (2014) 625–656.
[8] S.S. Datta, A.M. Ardekani, P.E. Arratia, A.N. Beris, I. Bischofberger, G.H. McKinley, J.G. Eggers, J.E. López-Aguilar, S.M. Fielding, A. Frishman, et al., Perspectives on viscoelastic flow instabilities and elastic turbulence, Phys. Rev. Fluids 7 (8) (2022) 080701.
[9] H.A.C. Sánchez, M.R. Jovanović, S. Kumar, A. Morozov, V. Shankar, G. Subramanian, H.J. Wilson, Understanding viscoelastic flow instabilities: Oldroyd-B and beyond, J. Non-Newton. Fluid Mech. (2022) 104742.
[10] D. Samanta, Y. Dubief, M. Holzner, C. Schäfer, A.N. Morozov, C. Wagner, B. Hof, Elasto-inertial turbulence, Proc. Natl. Acad. Sci. USA 110 (26) (2013) 10557–10562.
[11] Y. Dubief, V.E. Terrapon, J. Soria, On the mechanism of elasto-inertial turbulence, Phys. Fluids 25 (11) (2013) 110817.
[12] S. Sid, V.E. Terrapon, Y. Dubief, Two-dimensional dynamics of elasto-inertial turbulence and its role in polymer drag reduction, Phys. Rev. Fluids 3 (1) (2018) 1–10.
[13] G.H. Choueiri, J.M. Lopez, A. Varshney, S. Sankar, B. Hof, Experimental observation of the origin and structure of elastoinertial turbulence, Proc. Natl. Acad. Sci. 118 (45) (2021) e2102350118.
[14] A. Shekar, R.M. McMullen, S.-N. Wang, B.J. McKeon, M.D. Graham, Critical-layer structures and mechanisms in elastoinertial turbulence, Phys. Rev. Lett. 122 (2019) 124503.
[15] A. Shekar, R.M. McMullen, B.J. McKeon, M.D. Graham, Self-sustained elastoinertial Tollmien–Schlichting waves, J. Fluid Mech. 897 (2020) A3.
[16] A. Shekar, R.M. McMullen, B.J. McKeon, M.D. Graham, Tollmien-Schlichting route to elastoinertial turbulence in channel flow, Phys. Rev. Fluids 6 (9) (2021) 093301.
[17] R.J. Deissler, Noise-sustained structure, intermittency, and the Ginzburg-Landau equation, J. Stat. Phys. 40 (3) (1985) 371–395.
[18] P. Huerre, P.A. Monkewitz, Local and global instabilities in spatially developing flows, Annu. Rev. Fluid Mech. 22 (1) (1990) 473–537.
[19] G. Hariharan, M.R. Jovanović, S. Kumar, Spatio-temporal impulse responses in channel flow of viscoelastic fluids, in: 2018 Annual American Control Conference, ACC, IEEE, 2018, pp. 2857–2862.
[20] R. Shnapp, V. Steinberg, Splitting of localized disturbances in viscoelastic channel flow, J. Fluid Mech. 941 (2022) R3.
[21] P. Garg, I. Chaudhary, M. Khalid, V. Shankar, G. Subramanian, Viscoelastic pipe flow is linearly unstable, Phys. Rev. Lett. 121 (2) (2018) 24502.
[22] M. Khalid, I. Chaudhary, P. Garg, V. Shankar, G. Subramanian, The centre-mode instability of viscoelastic plane Poiseuille flow, J. Fluid Mech. 915 (2021) A43.
[23] I. Chaudhary, P. Garg, G. Subramanian, V. Shankar, Linear instability of viscoelastic pipe flow, J. Fluid Mech. 908 (2021) A11.
[24] D. Wan, G. Sun, M. Zhang, Subcritical and supercritical bifurcations in axisymmetric viscoelastic pipe flows, J. Fluid Mech. 929 (2021) A16.
[25] M. Zhang, Energy growth in subcritical viscoelastic pipe flows, J. Non-Newton. Fluid Mech. 294 (2021) 104581.
[26] M. Dong, M. Zhang, Asymptotic study of linear instability in a viscoelastic pipe flow, J. Fluid Mech. 935 (2022) A28.
[27] D. Wan, M. Dong, M. Zhang, On the large-Weissenberg-number scaling laws in viscoelastic pipe flows, J. Fluid Mech. 944 (2022) A21.
[28] J. Page, Y. Dubief, R.R. Kerswell, Exact traveling wave solutions in viscoelastic channel flow, Phys. Rev. Lett. 125 (2020) 154501.
[29] G. Buza, M. Beneitez, J. Page, R.R. Kerswell, Finite-amplitude elastic waves in viscoelastic channel flow from large to zero Reynolds number, J. Fluid Mech. 951 (2022) A3.
[30] G. Buza, J. Page, R.R. Kerswell, Weakly nonlinear analysis of the viscoelastic instability in channel flow for finite and vanishing Reynolds numbers, J. Fluid Mech. 940 (2022) A11.
[31] A. Morozov, Coherent structures in plane channel flow of dilute polymer solutions with vanishing inertia, Phys. Rev. Lett. 129 (1) (2022) 017801.
[32] M. Khalid, V. Shankar, G. Subramanian, Continuous pathway between the elasto-inertial and elastic turbulent states in viscoelastic channel flow, Phys. Rev. Lett. 127 (2021) 134502.
[33] R.J. Briggs, Electron-Stream Interaction with Plasmas, MIT-Press, 1964.
[34] P.K. Ray, T.A. Zaki, Absolute/convective instability of planar viscoelastic jets, Phys. Fluids 27 (1) (2015) 014110.
[35] S. Sircar, D. Bansal, Spatiotemporal linear stability of viscoelastic free shear flows: Dilute regime, Phys. Fluids 31 (8) (2019) 084104.
[36] N. Phan-Thien, R.I. Tanner, A new constitutive equation derived from network theory, J. Non-Newton. Fluid Mech. 2 (4) (1977) 353–365.
[37] D. Bansal, D. Ghosh, S. Sircar, Spatiotemporal linear stability of viscoelastic free shear flows: Nonaffine response regime, Phys. Fluids 33 (5) (2021) 054106.
[38] S.d.C. Hirata, L.d.B. Alves, N. Delenda, M. Ouarzazi, Convective and absolute instabilities in Rayleigh–Bénard–Poiseuille mixed convection for viscoelastic fluids, J. Fluid Mech. 765 (2015) 167–210.
[39] B. Qin, P.F. Salipante, S.D. Hudson, P.E. Arratia, Upstream vortex and elastic wave in the viscoelastic flow around a confined cylinder, J. Fluid Mech. 864 (2019) R2.
[40] R.B. Bird, C.F. Curtiss, R.C. Armstrong, O. Hassager, Dynamics of Polymeric Liquids, Volume 2: Kinetic Theory, Wiley, 1987.
[41] R. Bird, P. Dotson, N. Johnson, Polymer solution rheology based on a finitely extensible bead-spring chain model, J. Non-Newton. Fluid Mech. 7 (2–3) (1980) 213–235.
[42] Y. Dubief, C.M. White, V.E. Terrapon, E.S. Shaqfeh, P. Moin, S.K. Lele, On the coherent drag-reducing and turbulence-enhancing behaviour of polymers in wall flows, J. Fluid Mech. 514 (2004) 271–280.
[43] M. Zhang, I. Lashgari, T.A. Zaki, L. Brandt, Linear stability analysis of channel flow of viscoelastic Oldroyd-B and FENE-P fluids, J. Fluid Mech. 737 (2013) 249–279.
[44] J.M. Lopez, G.H. Choueiri, B. Hof, Dynamics of viscoelastic pipe flow at low Reynolds numbers in the maximum drag reduction limit, J. Fluid Mech. 874 (2019) 699–719.
[45] D. Cruz, F. Pinho, P.J. Oliveira, Analytical solutions for fully developed laminar flow of some viscoelastic liquids with a Newtonian solvent contribution, J. Non-Newton. Fluid Mech. 132 (1–3) (2005) 28–35.
[46] A. Bistagnino, G. Boffetta, A. Celani, A. Mazzino, A. Puliafito, M. Vergassola, Nonlinear dynamics of the viscoelastic Kolmogorov flow, J. Fluid Mech. 590 (2007) 61–80.

[47] P. Huerre, P.A. Monkewitz, Absolute and convective instabilities in free shear layers, J. Fluid Mech. 159 (1985) 151–168.
[48] S.A. Suslov, Numerical aspects of searching convective/absolute instability transition, J. Comput. Phys. 212 (1) (2006) 188–217.
[49] R.J. Deissler, The convective nature of instability in plane Poiseuille flow, Phys. Fluid 30 (8) (1987) 2303–2305.
[50] Z. Gao, A. Sergent, B. Podvin, S. Xin, P. Le Quéré, L.S. Tuckerman, Transition to chaos of natural convection between two infinite differentially heated vertical plates, Phys. Rev. E 88 (2) (2013) 023010.
[51] J. Tao, F. Zhuang, Absolute and convective instabilities of the natural convection in a vertical heated slot, Phys. Rev. E 62 (6) (2000) 7957.
[52] S.A. Suslov, S. Paolucci, Stability of non-Boussinesq convection via the complex Ginzburg–Landau model, Fluid Dyn. Res. 35 (3) (2004) 159.
[53] Z. Feng, D. Wan, M. Zhang, B.-F. Wang, Nonlinear spatiotemporal instabilities in two-dimensional electroconvective flows, Phys. Rev. Fluids 7 (2) (2022) 023701.
[54] J.T. Stuart, On the non-linear mechanics of wave disturbances in stable and unstable parallel flows Part 1. The basic behaviour in plane Poiseuille flow, J. Fluid Mech. 9 (3) (1960) 353–370.
[55] K. Stewartson, J.T. Stuart, A non-linear instability theory for a wave system in plane Poiseuille flow, J. Fluid Mech. 48 (3) (1971) 529–545.
[56] K. Fujimura, The equivalence between two perturbation methods in weakly nonlinear stability theory for parallel shear flows, Proc. R. Soc. London. A. Math. Phys. Sci. 424 (1867) (1989) 373–392.
[57] J. Watson, On the nonlinear mechanics of wave disturbances in stable and unstable parallel flows, J. Fluid Mech. 9 (3) (1960) 371–389.
[58] T. Herbert, Nonlinear stability of parallel flows by high-ordered amplitude expansions, AIAA J. 18 (3) (1980) 243–248.
[59] P. Sen, D. Venkateswarlu, On the stability of plane Poiseuille flow to finite-amplitude disturbances, considering the higher-order Landau coefficients, J. Fluid Mech. 133 (1983) 179–206.
[60] A.N. Morozov, W. van Saarloos, Subcritical finite-amplitude solutions for plane Couette flow of viscoelastic fluids, Phys. Rev. Lett. 95 (2005) 024501.
[61] K.G. Pham, S.A. Suslov, On the definition of Landau constants in amplitude equations away from a critical point, R. Soc. Open Sci. 5 (11) (2018) 180746.
[62] J. Cudby, A. Lefauve, Weakly nonlinear Holmboe waves, Phys. Rev. Fluids 6 (2) (2021) 024803.
[63] I. Delbende, J.-M. Chomaz, Nonlinear convective/absolute instabilities in parallel two-dimensional wakes, Phys. Fluids 10 (11) (1998) 2724–2736.
[64] C. Cossu, J.-M. Chomaz, D.S. Henningson, 2D nonlinear front propagation in the Blasius boundary layer, in: APS Division of Fluid Dynamics Meeting Abstracts, Vol. 54, 2001, pp. AM–001.
[65] J.-M. Chomaz, Transition to turbulence in open flows: what linear and fully nonlinear local and global theories tell us, Eur. J. Mech. B Fluids 23 (3) (2004) 385–399.
[66] M. Zhang, Weakly nonlinear stability analysis of subcritical electrohydrodynamic flow subject to strong unipolar injection, J. Fluid Mech. 792 (2016) 328–363.
[67] J. Chomaz, Absolute and convective instabilities in nonlinear systems, Phys. Rev. Lett. 69 (13) (1992) 1931–1934.
[68] J. Crouch, T. Herbert, A note on the calculation of Landau constants, Phys. Fluids A 5 (1) (1993) 283–285.